Materials Today Electronics 8 (2024) 100090

Contents lists available at ScienceDirect

Materials Today Electronics

journal homepage: www.elsevier.com/locate/mtelec

Cation doping strategy for improved carrier mobility and stability in metal-oxide Heterojunction thin-film transistors

Boyeon Park [a], San Nam [a], Youngjin Kang [a], Seong-Pil Jeon [b], Jeong-Wan Jo [c], Sung Kyu Park [b,*], Yong-Hoon Kim [a,*]

[a] School of Advanced Materials Science and Engineering, Sungkyunkwan University, Suwon 16419, Republic of Korea
[b] School of Electrical and Electronics Engineering, Chung-Ang University, Seoul 06974, Republic of Korea
[c] Electrical Engineering Division, Department of Engineering, University of Cambridge, Cambridge CB2 1TN, United Kingdom

ARTICLE INFO

Keywords:
Amorphous oxide semiconductor
Cation doping
Heterojunction channel
Energy band engineering
Passivation effect

ABSTRACT

The heterojunction channel architecture has emerged as a viable solution to enhance the performance of metal-oxide thin-film transistors (TFTs), addressing the performance limitations of single-channel counterparts. However, carrier mobility enhancement through a channel thickness design often encounters significant challenges such as the negative threshold voltage (V_{th}) shift. In this study, we present a cation doping strategy, designed to regulate V_{th} shift while simultaneously boosting carrier mobility in zinc-tin-oxide (ZTO)-based heterojunction TFTs. A comprehensive investigation of ZTO-based semiconductors was conducted to explore the impact of cation doping on the energy band structure and to find an optimal heterojunction channel structure for high carrier mobility and stability. The resulting ZTO/Ti-doped ZTO (Ti:ZTO) heterojunction TFTs demonstrated a field-effect mobility of 39.7 cm^2/Vs, surpassing the performance of ZTO TFTs (16.1 cm^2/Vs), with a minimal change in the V_{th}. Furthermore, the ZTO/Ti:ZTO TFTs exhibited enhanced bias-stress stability compared to the ZTO TFTs. We attribute the improved mobility and stability to the electron accumulation near the oxide channel heterointerface facilitated by band bending and defect passivation effect arising from the Ti:ZTO back-channel layer, respectively.

Introduction

Amorphous oxide semiconductors (AOSs) have attracted attention for use in various electronic devices due to their advantages such as high uniformity, low leakage current, and decent stability [1,2]. To date, indium-zinc-tin-oxide (IZTO), and indium-gallium-tin-oxide (IGTO) have been widely investigated for AOSs along with indium-based multi-cationic channels such as indium-gallium-zinc-oxide (IGZO) [2–5]. The incorporation of indium in the multi-cationic AOS channels can enhance the carrier mobility by lowering the effective electron mass [6]. However, it may cause deterioration of stability by the formation of oxygen vacancies from the weakly bonded In-O species [7,8]. Also, a considerable negative threshold voltage (V_{th}) shift may occur with high In content [9]. To suppress the oxygen vacancy formation, the influences of metal dopants with high oxygen bonding strength have been investigated. In fact, the addition of dopants such as Zr, Hf, and Ti, which act as carrier suppressors, can effectively control the oxygen vacancy formation and improve the bias-stress stability [10–12]. Despite this, the introduction of carrier suppressors can decrease the carrier mobility. Such a trade-off between the electrical performance and bias stability has emerged as a major challenge in the overall performance and stability of In-based AOSs [13]. A heterojunction active-channel structure can be a promising solution to address this limitation [14–17]. Enhanced charge transport properties can be obtained by configuring two channel layers with a large difference in Fermi level and band gap, possibly due to the energy band bending and charge confinement at the heterointerface [18]. For instance, In_2O_3/ZnO and IGZO/IZTO heterojunction thin-film transistors (TFTs) have shown enhanced electron mobility and high on-current density compared to single-channel TFTs [19,20].

Although energy band engineering is a practical pathway for enhancing device performance, the specific physical origins of increased mobility remain controversial. For instance, Lin et al. claimed that the improvement in electron mobility originates from the presence of quasi-two-dimensional electron gas (2DEG) at the oxide heterointerfaces [21]. Another possible reason for the increased mobility is the improved conduction pathway for electrons using back-channel layer with lower

* Corresponding authors.
E-mail addresses: skpark@cau.ac.kr (S.K. Park), yhkim76@skku.edu (Y.-H. Kim).

https://doi.org/10.1016/j.mtelec.2024.100090
Received 9 January 2024; Received in revised form 18 February 2024; Accepted 11 March 2024
Available online 16 March 2024

oxygen vacancy due to the defect passivation effect. In this case, an oxygen compensated-ITZO/uncompensated-ITZO bilayer channel structure is used [22]. The oxygen atoms have been proposed to diffuse from oxygen compensated-ITZO layer to the oxygen-uncompensated ITZO layer, causing reduced oxygen vacancies and hydroxyl concentrations at the ITZO/SiO_2 interface. Furthermore, the oxygen compensated-ITZO layer can act as a barrier, preventing the penetration of ambient oxygen and water molecules into the channel layer. Nonetheless, a comprehensive investigation of the physical origins of the performance enhancement in oxide heterojunction TFTs is necessary. Additionally, In is a rare-earth element and poses significant cost and toxicity challenges, limiting its widespread application. Consequently, there is a pressing need for the development of In-free AOSs capable of offering cost-effectiveness, high performance, and environmental safety [23]. Among these candidates, zinc-tin-oxide (ZTO) is promising due to its high carrier mobility and relatively high bond dissociation energy of Sn-O (~548 kJ/mol) [24,25]. However, the oxygen vacancies in ZTO can still function as defect states, degrading stability. Therefore, proper cation doping is essential to regulate and suppress the formation of oxygen vacancies. For the dopant in ZTO, Ti was selected since it has relatively high Ti-O bond dissociation energy (672.4 kJ/mol) [26], and TiO_2 shows relatively low deposition rate compared to ZTO, which can lead to a facile control of Ti doping concentration in ZTO film by a co-sputtering process.

Here, we performed an in-depth investigation of ZTO-based AOSs to analyze the influence of cation doping on the energy band structure and to determine the optimal heterojunction channel structure to achieve enhanced performance and stability. We implemented amorphous ZTO/Ti-doped ZTO (Ti:ZTO) heterojunctions as the channel structure. Specifically, the Ti doping concentration in Ti:ZTO was intentionally controlled using a co-sputtering process to manipulate the energy band structure at the heterointerface. Based on the energy band structures, we designed heterojunction channel layers with a large difference in work function, which leads to electron accumulation near the oxide heterointerface. We investigated electrical performance and bias-stress stability for optimized heterojunction TFTs. Moreover, we discuss the underlying physical origin for the enhanced mobility and bias stability.

Experimental details

Device fabrication

A heavily doped p-type silicon (p-Si) wafer with a 200-nm-thick silicon dioxide (SiO_2) layer was used as a substrate. The p-Si served as the gate electrode and the SiO_2 served as the gate insulator. The substrate was cleaned with acetone and isopropyl alcohol for 10 min each. Then, ZTO and Ti:ZTO channel layers were deposited by radio-frequency (RF) magnetron sputtering. For the Ti:ZTO layer, a co-sputtering process was used employing ZTO and TiO_2 targets. The Zn:Sn atomic composition ratio of ZTO target was 7:3. The RF power for ZTO varied as 50, 100, and 150 W. Also, the RF power for TiO_2 varied as 0, 50, 100, and 150 W. During the RF magnetron sputtering, the base and working pressure was 2×10^{-6} mTorr and 2×10^{-3} mTorr, respectively (Ar/O_2 ratio: 18/2 sccm). The deposited channel layers were annealed on a hot plate at 450 °C for 1 h in an air ambient. The channel layers were patterned using a lift-off process. Afterward, 40-nm-thick indium-tin-oxide source/drain electrodes were deposited by sputtering and patterned using a lift-off process (channel width = 200 μm, length = 50 μm).

Film and device characterization

To examine the crystalline structures of ZTO and Ti:ZTO films, grazing incidence X-ray diffraction was carried out with a grazing angle of 0.5° (GIXRD, Rigaku, SmartLAB). The optical transmittance of ZTO and Ti:ZTO films was measured using an UV/vis-NIR spectrophotometer (UV/vis, Cary 5000, Agilent Technologies). The work function (φ), gap between the Fermi level (E_F), and valence band maximum (E_{VBM}) of the films were analyzed using ultraviolet photoelectron spectroscopy (UPS, ESCALAB250, Thermo-Scientific) with a He I source of 21.2 eV. The chemical compositions and binding states of the films were analyzed using X-ray photoelectron spectroscopy (XPS, ESCALAB250Xi, Thermo-Scientific) with a monochromatic Al Kα radiation source of 1486.6 eV. The binding energy in the XPS spectra was calibrated using the C 1 s peak at 284.5 eV. The XPS depth profile for ZTO/Ti:ZTO heterojunction samples was performed using Ar^+ ion gun etching. The electrical characteristics of single-layer ZTO and heterojunction TFTs were measured using a semiconductor parameter analyzer (Agilent 4155C, Agilent Technologies) in a dark ambient. Additionally, the gate-bias stability was measured by applying a gate bias (V_G) of ±20 V and drain bias (V_D) of 0.1 V for a duration of 5760 s.

Results and discussion

Energy band structures of ZTO and Ti:ZTO films

The device structure of ZTO/Ti:ZTO heterojunction TFTs is shown in Fig. 1a. The TFT consists of a bilayer channel including undoped ZTO and Ti:ZTO layers. Undoped ZTO, which is adjacent to the gate insulator, was used as the front-channel layer to obtain high carrier mobility since the carrier concentration tends to decrease with the Ti doping [27]. Generally, the decrease in oxygen vacancies can lead to a reduction of carrier concentration, and the Ti dopants with strong oxygen bonding strength can suppress the formation of oxygen vacancies which can act as shallow or deep traps in the channel layer [26]. As a result, the Ti:ZTO is used as the back-channel layer. A co-sputtering process was utilized to control the Ti doping concentration in ZTO. Specifically, the Ti concentration was controlled by adjusting the sputtering power for ZTO and TiO_2 during the deposition. Fig. 1b shows the Ti concentration as a function of TiO_2 sputtering power (P_{TiO2}) with a fixed ZTO sputtering power (P_{ZTO}) at 150 W. As displayed, the Ti concentration monotonously increased with P_{TiO2} in the range of 0–2.21 at.%. Furthermore, the optical properties, such as the optical bandgap (E_{opt}), varied with Ti doping. **Fig. S1a-c** show the optical transmittance spectra of ZTO and Ti:ZTO films deposited at different P_{TiO2} (0, 50, 100, and 150 W) when the P_{ZTO} is fixed at 150, 100 or 50 W. All the films exhibited average transmittance over 80% in the visible light region (λ = 400–800 nm). The E_{opt} values were obtained from the Tauc plots (**Fig. S1d-f**) using the equation,

$$\alpha h\nu = A\left(h\nu - E_{opt}\right)^n \quad (1)$$

where α is the absorption coefficient, hυ is the photon energy, and A is a constant. The best linear part of the Tauc plot was obtained for $n = 2$, implying the direct band gap transition. The E_{opt} values as a function of P_{TiO2} with fixed P_{ZTO} are shown in Fig. 1c. As indicated, the E_{opt} of Ti:ZTO films exhibited an increasing trend with the P_{TiO2}. For instance, the undoped ZTO film deposited with P_{ZTO} of 150 W showed E_{opt} of 3.86 eV. Meanwhile, the Ti:ZTO films co-sputtered with P_{TiO2} of 50, 100, and 150 W showed E_{opt} values of 4.01, 4.10, and 4.17 eV, respectively.

Nevertheless, it has been argued that the formation of quasi-2DEG or a potential well in the heterojunction channel, resulting from the Fermi level alignment, is mainly attributed to the enhanced electrical performance [18]. Field-effect mobility can be increased by the formation of quasi-2DEG or a potential well with high electron concentration due to the transition in the conduction mechanism from trap-limited conduction to percolation conduction [21]. To obtain heterostructure TFTs with a quasi-2DEG or a potential well, we first investigated the energy band structures of undoped ZTO and Ti:ZTO films. In particular, the gap between the Fermi level and valence band maximum (E_F - E_{VBM}), the gap between the conduction band minimum and Fermi level (E_{CBM} - E_F), and the work function (φ) were determined from UPS analysis (**Fig. S2**).

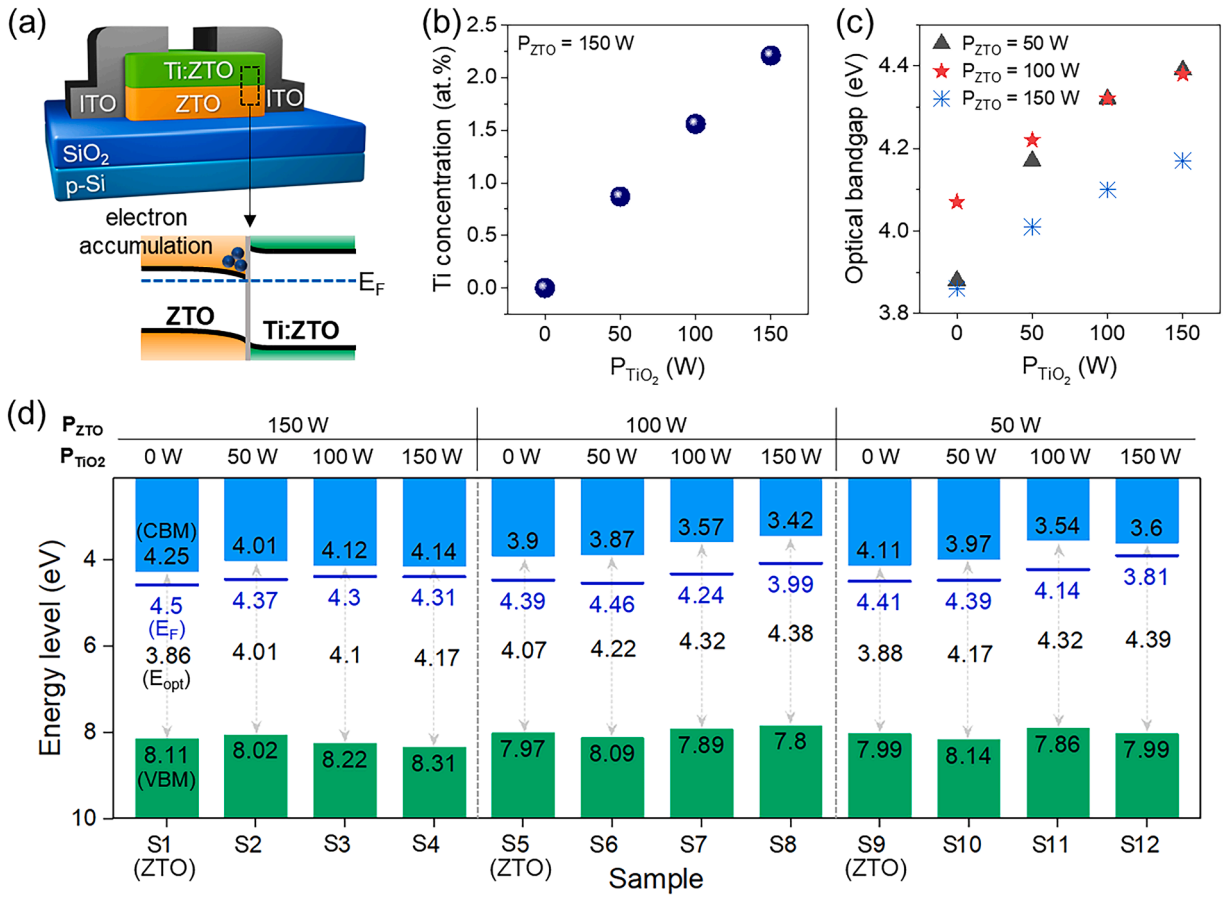

Fig. 1. (a) Device and energy band structure of ZTO/Ti:ZTO heterojunction TFTs. (b) Ti concentration as a function of P_{TiO2} with fixed P_{ZTO} of 150 W. (c) Optical band gap as a function of P_{TiO2} with fixed P_{ZTO}. (d) Schematic energy band structures of ZTO and Ti:ZTO films with different sputtering power combinations.

Based on the UV/vis and UPS analysis, the energy levels of CBM and VBM for ZTO and Ti:ZTO films were obtained as depicted in Fig. 1d. Also, the E_{opt}, E_F - E_{VBM}, E_{CBM} - E_F, φ, and electron affinity (χ) are summarized in **Table S1**. The sample numbers in Fig. 1d and **Table S1** indicate the sample names with various sputtering power combinations of P_{ZTO} and P_{TiO2}. Combinations with a fixed P_{ZTO} of 150 W and P_{TiO2} values of 0, 50, 100, and 150 W are denoted as S1, S2, S3, and S4, respectively. Similarly, S5, S6, S7, and S8 denote combinations with a fixed P_{ZTO} of 100 W and P_{TiO2} values of 0, 50, 100, and 150 W, respectively. Also, S9, S10, S11, and S12 denote the combinations with a fixed P_{ZTO} of 50 W and P_{TiO2} values of 0, 50, 100, 150 W, respectively. Overall, the E_F - E_{VBM} of Ti:ZTO films increased with the P_{TiO2}. For example, the undoped ZTO film (S1, P_{ZTO} = 150 W) exhibited E_F - E_{VBM} of 3.61 eV, while it increased to 3.65 (S2), 3.92 (S3), and 4.00 eV (S4) as the P_{TiO2} increased to 50, 100, and 150 W, respectively. Additionally, the φ showed a decreasing trend with P_{TiO2} (Ti concentration). Furthermore, Ti doping in the ZTO film did not result in the formation of any observable secondary phases. Both the undoped ZTO and Ti-doped ZTO films exhibited amorphous structures, as shown in the GIXRD patterns (**Fig. S3**).

Notably, the E_{opt} and E_{VBM} values of Ti:ZTO films increase with P_{TiO2}. The widening of the band gap is generally explained by the Burstein-Moss (BM) shift [28–30], quantum confinement effect [31], compressive stress [32], or addition of materials with a larger band gap [33]. First, it is unlikely that BM shift is the main cause for the widening of band gap since the Ti atoms generally act as oxygen vacancy suppressor due to the strong Ti-O bonding strength [26,27]. According to the equation for BM shift (ΔBM) [34],

$$\Delta BM = \frac{\hbar^2}{2m^*}\left(3\pi^2 n_e\right)^{2/3} \quad (2)$$

where $\hbar$ is the Planck constant, m* is the reduced mass, and n_e is the electron concentration. As shown in Eq. (2), the ΔBM increases with electron concentration. However, the electron concentration would decrease with Ti doping, which would not explain the widening of the band gap with Ti doping. Also, the effects on compressive stress can be neglected due to the low Ti concentrations in the Ti:ZTO film. Instead, there is a possible reason for the band gap tuning with Ti doping regarding the correlation between the band gap and oxygen vacancy. It has been proposed that when a large number of oxygen vacancies exists, the oxygen vacancy states become more delocalized, overlapping with the valence band edge, raising the position of the valence band and decreasing the band gap [35,36]. Fig. 2a-d show the O 1 s core-level spectra of S1~S4 samples (P_{ZTO} = 150 W, P_{TiO2} = 0, 50, 100, and 150 W). Each O 1 s peak was deconvoluted into three sub-peaks centered at around 530.4 ± 0.1 eV, 531.1 ± 0.1 eV, and 532.2 eV, which are associated with oxygen lattice (M-O), oxygen vacancies (V_O), and oxygen in hydroxyl groups (M-OH), respectively [37]. In particular, the V_O-related peak can be attributed to the loss of oxygen or formation of oxygen vacancies in the film [38]. According to the results, the area ratio of V_O decreased from 25.3% for S1 to 19.7% for S4, as the P_{TiO2} increases (with the increase of Ti concentration from 0 to 2.21 at.%) (Fig. 2e). In contrast, the area ratio of M-O increased from 67.8% for S1 to 74% for S4. Meanwhile, the area ratio of M-OH was almost unchanged. These results would explain the role of Ti as an oxygen vacancy suppressor, as mentioned above. Furthermore, the results suggest that oxygen vacancy states which exist in the deep level near the valence band edge decreased

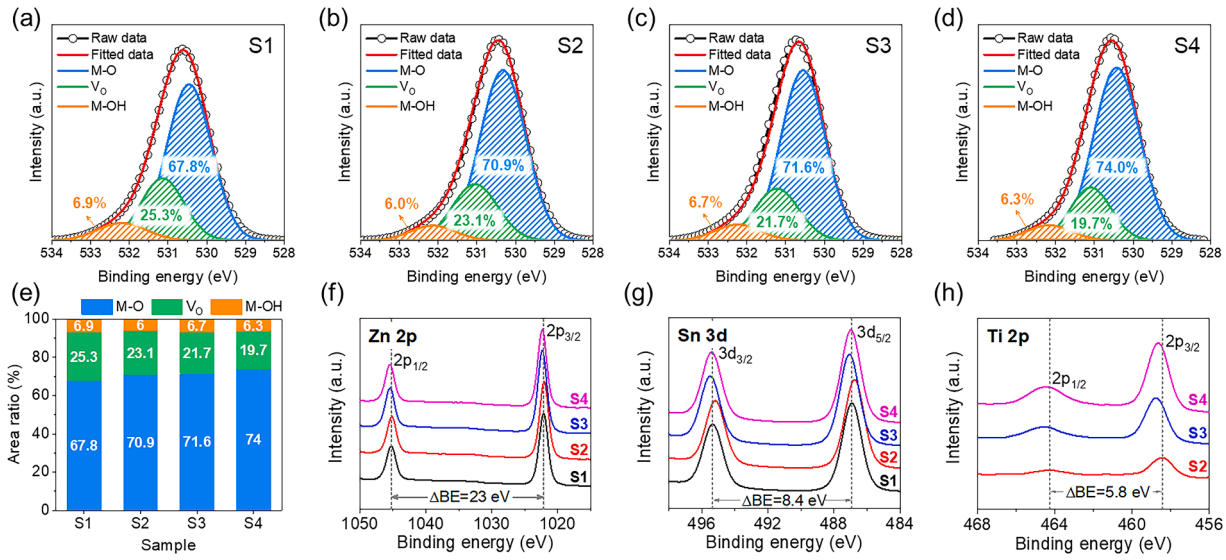

Fig. 2. XPS O 1 s spectra of samples (a) S1, (b) S2, (c) S3, and (d) S4. (e) Area ratio of oxygen lattice (M-O), oxygen vacancies (V_O), and oxygen in hydroxyl groups (M-OH) in samples of S1~S4. XPS core-level spectra of (f) Zn 2p, (g) Sn 3d, and (h) Ti 2p for S1~S4 samples.

with Ti doping [35,39]. Thus, we speculated that the band gap widening of Ti:ZTO films with higher Ti concentration is due to the decreased impurity states created from the oxygen vacancies.

Additionally, Fig. 2f-h show the XPS core-level spectra of Zn 2p, Sn 3d, and Ti 2p for samples S1 to S4. Also, the estimated atomic compositions for Zn, Sn, Ti, and O are summarized in **Table S2**. For the S1 sample (undoped ZTO, $P_{ZTO} = 150$ W), the Zn $2p_{3/2}$ peak was positioned at 1022.2 eV with a spin orbit splitting of ~23 eV. The Sn $3d_{5/2}$ peak position was at 486.9 eV with a spin orbit splitting of 8.4 eV, indicating the Sn^{4+} ionic states [40]. Also, the Ti $2p_{3/2}$ peak was observed at 458.5 eV with a spin orbit splitting of 5.8 eV, showing the Ti^{4+} ionic states [41]. As for the Ti:ZTO films, the peak positions of Zn 2p, Sn 3d, and Ti 2p generally showed a shift toward higher binding energies as the P_{TiO2} increased (from S1 to S4). These peak shifts likely result from the chemical shift due to the oxygen vacancies. Indeed, the oxygen vacancies can cause a peak shift toward lower binding energy states [42]. As mentioned, the number of oxygen vacancies decreased with the addition of Ti. Therefore, the peak shift toward higher binding energies is caused by the reduced number of oxygen vacancies with Ti doping.

Electrical characteristics of ZTO/Ti:ZTO heterojunction TFTs

To identify the distinct influence of heterojunction channel structure on device performance, we designed a heterojunction channel with a large difference in φ between the front and back-channel layers. In particular, we used ZTO with a P_{ZTO} of 150 W for the front-channel layer (S1, φ = 4.50 eV), and Ti:ZTO with P_{ZTO} of 100 W and P_{TiO2} of 150 W as the back-channel layer (S8, φ = 3.99 eV). The total channel thickness

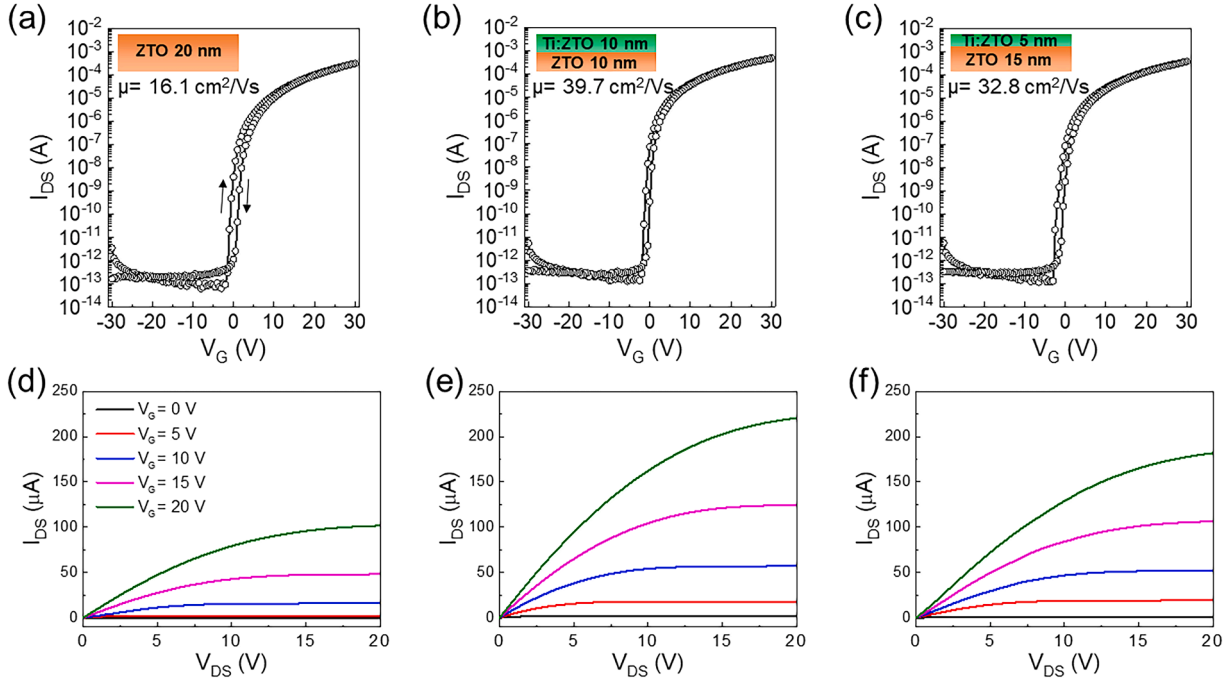

Fig. 3. Transfer and output characteristics of (a, d) single-layer ZTO TFT, (b, e) ZTO/Ti:ZTO TFT with $t_{ZTO} = 10$ nm and $t_{Ti:ZTO} = 10$ nm, and (c, f) ZTO/Ti:ZTO TFT with $t_{ZTO} = 15$ nm and $t_{Ti:ZTO} = 5$ nm.

was fixed at 20 nm. Fig. 3 shows the transfer (I_D–V_G) and output (I_D–V_D) characteristics of single-layer ZTO (S1) and ZTO/Ti:ZTO TFTs. The electrical properties are summarized in Table 1. The single-layer ZTO TFTs exhibited a saturation field-effect mobility (μ_{sat}) of 16.1 cm^2/Vs, which was calculated from the following equation,

$$\mu_{sat} = \left(\frac{d\sqrt{I_{DS}}}{dV_G}\right)^2 \frac{dI_{DS}}{dV_G}\frac{2L}{WC_i} \quad (3)$$

where C_i is capacitance per unit area, W is the channel width, and L is the channel length. Notably, in the heterojunction TFTs, the field-effect mobility significantly increased compared to single-layer ZTO TFTs, exhibiting μ_{sat} values of 39.7 and 32.8 cm^2/Vs when the t_{ZTO} values were 10 and 15 nm ($t_{Ti:ZTO}$ of 10 and 5 nm), respectively (Fig. 3b-c). This result can be attributed to the increased carrier concentration [43]. Additionally, the single-layer ZTO TFTs exhibited a clockwise hysteresis of 1.86 V (Table 1). In the case of heterojunction TFTs, the hysteresis was decreased, exhibiting hysteresis of 1.11 and 1.41 V with the t_{ZTO} of 10 and 15 nm ($t_{Ti:ZTO}$ of 10 and 5 nm), respectively. Also, the contact properties at the channel/electrode contacts were not altered by the presence of a Ti:ZTO back-channel layer as shown in the output curves (Fig. 3d-f). Furthermore, other sputtering power combinations for Ti:ZTO films were used to investigate the influence of back-channel deposition conditions on device performance. Specifically, we used 10-nm-thick ZTO for the front-channel layer, and 20-nm-thick Ti:ZTO with a fixed P_{ZTO} of 50 W and P_{TiO2} of 50 (S10), 100 (S11), and 150 W (S12) were employed for the back-channel layer (**Fig. S4**). As shown in **Fig. S4a-c**, the heterojunction TFTs with relatively higher P_{TiO2} compared to P_{ZTO} showed severe degradations in the electrical properties. Particularly, a significant decrease in mobility was observed, which can be attributed to the non-Ohmic contact at the channel/source-drain electrode junctions [44]. Clear evidence for non-Ohmic contact can be observed in the output characteristics in **Fig. S4f**, which shows a non-linear curvature in low drain voltage regions.

Bias-stress stability of ZTO/Ti:ZTO heterojunction TFTs

To gain further insight into the effectiveness of heterojunction channel structure on device reliability, we investigated the gate-bias stability of single-layer and heterojunction TFTs. We performed the positive gate-bias stress (PBS) and negative gate-bias stress (NBS) tests and Fig. 4a-c shows the evolution of transfer curves under PBS for single-layer ZTO and heterojunction TFTs. Also, Fig. 4d shows a V_{th} shift (ΔV_{th}) under PBS as a function of stress time. After the stress, a parallel V_{th} shift was observed without accompanying a significant change in μ_{sat}, SS, and on/off ratio. Notably, the single-layer ZTO TFT showed relatively poor stability, exhibiting a ΔV_{th} of 4.85 V after 5760 s of PBS. The ΔV_{th} was clearly improved by adopting the heterojunction structure. In particular, the ΔV_{th} was reduced to 2.9 and 3.59 V for heterojunction TFTs with t_{ZTO} values of 10 and 15 nm ($t_{Ti:ZTO}$ of 10 and 5 nm), respectively. Typically, the PBS-induced V_{th} variation is explained by the charge trapping model [14], in which ΔV_{th} occurs due to the trapping of charges into the channel and near the channel/gate insulator interface.

Table 1
Electrical properties of single-layer ZTO and ZTO/Ti:ZTO heterojunction TFTs.

Channel structure	μ_{sat} (cm^2/Vs)	SS (V/dec)	V_{th} (V)	$I_{on/off}$ (× 10^9)	hysteresis (V)
Single-layer ZTO	16.1	0.446	−0.28	3.28	1.86
ZTO/Ti:ZTO heterojunction (t_{ZTO} = 10 nm, $t_{Ti:ZTO}$ = 10 nm)	39.7	0.365	−0.99	3.43	1.11
ZTO/Ti:ZTO heterojunction (t_{ZTO} = 15 nm, $t_{Ti:ZTO}$ = 5 nm)	32.4	0.608	−1.56	2.95	1.41

Therefore, the improved PBS stability in heterojunction TFTs can be attributed to a decrease in interfacial trap density compared to that of single-layer ZTO TFTs [14].

Furthermore, the influence of a heterojunction channel structure on NBS stability was investigated. Single-layer ZTO TFTs exhibited a large ΔV_{th} of −8.05 V after the NBS of 5760 s (Fig. 4e). Overall, heterojunction TFTs showed improved NBS stability. The ΔV_{th} decreased to −2.48 and −2.49 V for heterojunction TFTs with t_{ZTO} values of 10 and 15 nm ($t_{Ti:ZTO}$ of 10 and 5 nm), respectively (Fig. 4f-h). Generally, the ΔV_{th} under NBS is closely related to the oxygen vacancy states and adsorbed species on the channel layer [14,45]. By lowering the E_F in channel region under NBS, the transition from V_O to V_O^{2+} can lead to a V_{th} shift toward the negative bias direction [46]. In the heterojunction channel structure, free electron density increases in the ZTO layer due to the transfer of electrons from Ti:ZTO to ZTO layer, which increases the formation energy of V_O. Thus, the reduction of V_O and trap density in the ZTO layer may lead to less charge trapping during NBS. Also, due to the addition of Ti in ZTO channel, the V_O generation can be suppressed in the Ti:ZTO back-channel layer and near the ZTO/Ti:ZTO heterointerface. Moreover, in the case of pristine ZTO, the surface states can be altered by the adsorption of moisture, O_2-related species, and organic residues from the photolithographic process [47–50]. Under NBS, these adsorbed impurities and V_O defects in ZTO can release electrons, forming a positive space charge, and lead to large negative V_{th} shift. Thus, the improvement in NBS stability resulted from the heterojunction TFTs with lower density of V_O in channels.

Mechanisms for enhanced electrical performance and bias stability

Several studies have reported that the mobility improvement in heterojunction TFTs can originate from the band-bending effect, which induces a high density of electron accumulation near the heterointerface and enhanced electron transport [18–21]. **Fig. S5** shows the schematic energy band diagram of ZTO/Ti:ZTO heterojunction channel. It can be inferred that the electron transfer from Ti:ZTO layer to ZTO layer induces the accumulation of free electrons in the ZTO layer near the heterointerface. Due to the effective band bending from the large difference in φ and smaller band gap of ZTO front-channel layer, higher density of electron accumulation can cause the dramatic improvement in mobility for the heterojunction TFTs. Additionally, the passivation effect arising from the top Ti:ZTO back-channel layer can be another possible reason for the enhanced mobility and stability. To elucidate the improved electrical performance using the heterojunction structure, we performed XPS depth profile measurements for the ZTO/Ti:ZTO heterojunction film. First, **Fig. S6a** shows the XPS depth profile of ZTO/Ti:ZTO heterojunction structure with t_{ZTO} and $t_{Ti:ZTO}$ values of 10 and 20 nm, respectively. At an etch time of ~150 s, the Ti 2p peak became almost indistinguishable, thus, we interpret this point as the back-channel/front-channel interface. Also, since the Zn 2p and Sn 3d peaks became almost indistinguishable at an etch time of 240 s, we interpret this point as the front-channel/Si interface. **Fig. S6b** shows the evolution of O 1 s XPS spectra according to the depth direction in the ZTO/Ti:ZTO channel. The O 1 s spectra with six splitting depth levels are summarized in **Table S3**. The positions of depth include the Ti:ZTO region, the interfacial Ti:ZTO/ZTO region, the ZTO region, and the interfacial ZTO/Si region. These six depth levels were fitted with three sub-peaks centered at binding energies of 530.2 ± 0.1, 531±0.3, and 532±0.3 eV, which are assigned to M-O, V_O, and M-OH, respectively. As shown in **Fig. S6b**, the areal ratio of V_O in the Ti:ZTO layer increased from 19.4% to 23.4% towards the heterointerface, while the M-O bonding ratio decreased from 75.9% to 71.2%. In contrast, the V_O ratio decreased from 24% to 21.9% in the ZTO front-channel layer near the heterointerface, suggesting redistribution of oxygen atoms within the ZTO/Ti:ZTO channel layers. It is understood that a higher ratio of M-O bonding states and a reduction of oxygen vacancies led to a better path for electron percolation conduction [46]. Thus, enhanced mobility of

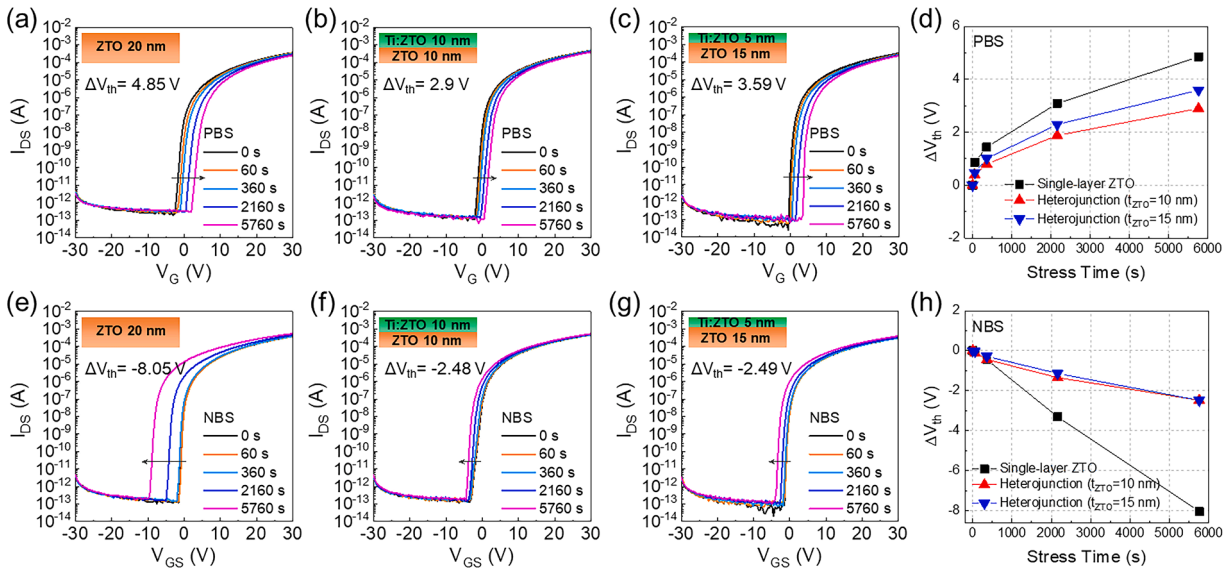

Fig. 4. Evolution of transfer curves for TFTs with different channel structures under PBS and NBS: (a, e) single-layer ZTO TFT, (b, f) ZTO/Ti:ZTO TFT with $t_{ZTO} = 10$ nm and $t_{Ti:ZTO} = 10$ nm, and (c, g) ZTO/Ti:ZTO TFT with $t_{ZTO} = 15$ nm and $t_{Ti:ZTO} = 5$ nm. Variations in V_{th} as a function of stress time for the single-layer ZTO and ZTO/Ti:ZTO TFTs under (d) PBS and (h) NBS.

ZTO/Ti:ZTO TFTs can be attributed to the reduced V_O ratio and increased M-O bonding states in the ZTO layer where the conduction channel is formed. It should be noted that the Ti:ZTO back-channel layer has a relatively small portion of oxygen vacancies compared to the ZTO front-channel layer (**Fig. S6b**), which implies that the Ti:ZTO layer can act as a passivation layer.

Additionally, the top Ti:ZTO back-channel layer stacked on the ZTO layer can function as a passivation layer that enhances the gate-bias stability. As shown in Fig. 4a and 4d, the single-layer ZTO TFTs are especially vulnerable to gate-bias stress mainly due to the high concentration of oxygen vacancies (area ratio of $V_O = 25.3\%$, Fig. 2a) [51]. The Ti:ZTO back-channel layer has a relatively lower concentration of oxygen vacancies compared to the ZTO front-channel layer. During the annealing process at 450 °C, oxygen atoms in the Ti:ZTO layer can diffuse into the ZTO layer and lower the number of oxygen vacancies, thereby enhancing the electrical performance and gate-bias stability (Fig. 5a). The diffusion of oxygen atoms into the ZTO layer near the heterointerface can be supported by the gradual decrease of V_O area ratio as shown in **Fig. S6b**. Furthermore, the surface of channel is sensitive to oxygen and moisture present in air [52]; this affects the electrical properties such as mobility and V_{th} [53]. In particular, oxide films with lower oxygen vacancies are more immune to gaseous species such as oxygen and moisture [22]. Therefore, the Ti:ZTO layer having fewer oxygen vacancies and positioned on top of the ZTO layer can effectively block the oxygen and moisture. This, in turn, can minimize the instability caused by the ambient gas.

To provide more details for the enhanced gate-bias stability with heterojunction structure, energy band diagrams for single-layer ZTO and ZTO/Ti:ZTO TFTs under PBS and NBS conditions are illustrated in Fig. 5b and 5c, respectively. As previously mentioned, the positive ΔV_{th} in single-layer ZTO TFTs is mainly due to electron trapping near the channel/gate insulator interface [14] and field-induced adsorption of ambient oxygen at the back-channel surface. In contrast, the Ti:ZTO layer with lower oxygen vacancies can reduce the absorption of oxygen at the surface and defects in the channel due to the reduced oxygen vacancies in ZTO/Ti:ZTO TFTs [22]. Hence, the positive V_{th} shift under

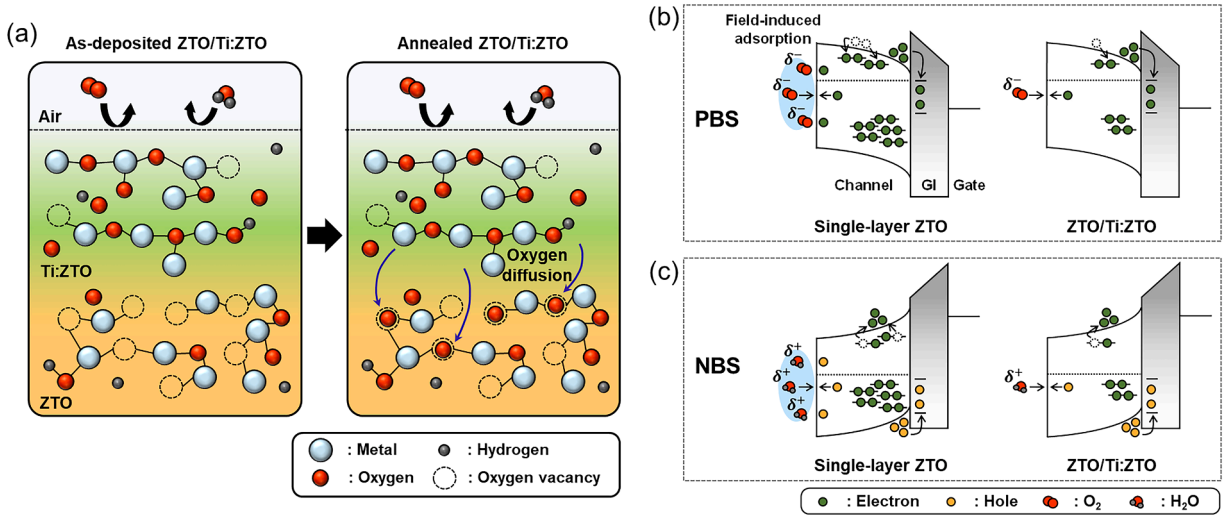

Fig. 5. (a) Schematic illustration of mechanism for oxygen diffusion in ZTO/Ti:ZTO heterojunction channel during the annealing process. Schematic energy band structures of single-layer ZTO and ZTO/Ti:ZTO TFTs under (b) PBS and (c) NBS conditions.

PBS can be suppressed with the ZTO/Ti:ZTO heterojunction channel, [54]. In the case of NBS, a higher concentration of V_O gives rise to larger negative V_{th} shift because the electrons are released from the V_O [14]. Also, the adsorption of H_2O molecules on the surface can capture the holes in the channel layer (Fig. 5c), causing a negative V_{th} shift. With the Ti:ZTO back-channel layer, we obtained improved stability in heterostructure TFTs due to the reduced V_O at the surface and heterointerface as shown in Fig. 5b and 5c.

Conclusions

In this study, ZTO-based heterojunction channel TFTs were investigated with the goal of obtaining high electrical performance and gate-bias stability. In particular, we designed a heterojunction channel with a large difference in work function by cation doping strategies using a co-sputtering method. The optimized ZTO/Ti:ZTO TFTs exhibited improved carrier mobility and gate-bias stability compared to single-layer ZTO TFTs. Furthermore, we provided a possible origin for enhanced mobility and stability. A ZTO/Ti:ZTO heterojunction channel with a large difference in work function can lead to effective band bending in the oxide heterojunction channel structure, leading to a higher electron accumulation near the heterointerface and increased carrier mobility. Additionally, the XPS depth profile results suggest the passivation effect from the Ti:ZTO back-channel layer. We envision that our heterojunction channel design concept can provide a potential approach for the development of high-performance AOS TFTs with high carrier mobility and gate-bias stability.

CRediT authorship contribution statement

Boyeon Park: Writing – original draft, Visualization, Methodology, Investigation, Formal analysis, Data curation, Conceptualization. **San Nam:** Methodology, Investigation, Data curation. **Youngjin Kang:** Methodology, Investigation. **Seong-Pil Jeon:** Methodology, Investigation. **Jeong-Wan Jo:** Methodology, Investigation, Formal analysis. **Sung Kyu Park:** Writing – original draft, Validation, Resources, Conceptualization. **Yong-Hoon Kim:** Writing – original draft, Visualization, Resources, Investigation, Funding acquisition, Formal analysis, Data curation, Conceptualization.

Declaration of competing interest

The authors declare that they have no known competing financial interests or personal relationships that could have appeared to influence the work reported in this paper.

Data availability

Data will be made available on request.

Acknowledgments

This research was supported by the Technology Innovation Program (20012617, Core technology evelopment of CMOS device fabrication using nonsilicon semiconductor thin-film transistors for high resolution large area display) funded by the Ministry of Trade, Industry & Energy (MOTIE, Korea), by the National Research Foundation of Korea (NRF) grant funded by the Korea Government (Ministry of Science and ICT) (No. NRF-2022R1A2C2010774), and by the GRRC program of Gyeonggi Province (GRRC Sungkyunkwan 2023-B04).

Supplementary materials

Supplementary material associated with this article can be found, in the online version, at doi:10.1016/j.mtelec.2024.100090.

References

[1] E. Fortunato, P. Barquinha, R. Martins, Oxide semiconductor thin-film transistors: a review of recent advances, Adv. Mater. 24 (2012) 2945–2986, https://doi.org/10.1002/adma.201103228.
[2] K. Nomura, H. Ohta, A. Takagi, T. Kamiya, M. Hirano, H. Hosono, Room-temperature fabrication of transparent flexible thin-film transistors using amorphous oxide semiconductors, Nature 432 (2004) 488–492, https://doi.org/10.1038/nature03090.
[3] S.H. Kim, C.H. Ahn, M.G. Yun, S.W. Cho, H.K. Cho, Anomalous tin chemical bonding in indium-zinc-tin oxide films and their thin film transistor performance, J. Phys. D: Appl. Phys. 47 (2014) 485101, https://doi.org/10.1088/0022-3727/47/48/485101.
[4] J. Lee, D. Kim, S. Lee, J. Cho, H. Park, J. Jang, High field effect mobility, amorphous In-Ga-Sn-O thin-film transistor with no effect of negative bias illumination stress, IEEE Electron Device Lett 40 (2019) 1443–1446, https://doi.org/10.1109/LED.2019.2931089.
[5] J. Sheng, T.H. Hong, H.-M. Lee, K.R. Kim, M. Sasase, J. Kim, H. Hosono, J.-S. Park, Amorphous IGZO TFT with high mobility of ~70 cm2/(Vs) via vertical dimension control using PEALD, ACS Appl. Mater. Interfaces 11 (2017) 40300–40309, https://doi.org/10.1021/acsami.9b14310.
[6] J.-Y. Noh, H. Kim, H.-H. Nahm, Y.-S. Kim, D.H. Kim, B.-D. Ahn, J.-H. Lim, G. H. Kim, J.-H. Lee, J. Song, Cation composition effects on electronic structures of In-Sn-Zn-O amorphous semiconductors, J. Appl. Phys. 113 (2013) 183706, https://doi.org/10.1063/1.4803706.
[7] J.K. Jeong, J.H. Jeong, H.W. Yang, J.-S. Park, Y.-G. Mo, H.D. Kim, High performance thin film transistors with cosputtered amorphous indium gallium zinc oxide channel, Appl. Phys. Lett. 91 (2007) 113505, https://doi.org/10.1063/1.2783961.
[8] J.H. Baek, H. Seol, K. Cho, H. Yang, J.K. Jeong, Comparative study of antimony doping effects on the performance of solution-processed ZIO and ZTO field-effect transistors, ACS Appl. Mater. Interfaces 9 (2017) 10904–10913, https://doi.org/10.1021/acsami.7b01090.
[9] M.H. Cho, M.J. Kim, H. Seul, P.S. Yun, J.U. Bae, K.-S. Park, J.K. Jeong, Impact of cation compositions on the performance of thin-film transistors with amorphous indium gallium zinc oxide grown through atomic layer deposition, J. Inf. Disp. 20 (2019) 73–80, https://doi.org/10.1080/15980316.2018.1540365.
[10] J.-S. Park, K.S. Kim, Y.-G. Park, Y.-G. Mo, H.D. Kim, J.K. Jeong, Novel ZrInZnO thin-film transistor with excellent stability, Adv. Mater. 21 (2009) 329–333, https://doi.org/10.1002/adma.200802246.
[11] C.-J. Kim, S. Kim, J.-H. Lee, J.-S. Park, S. Kim, J. Park, E. Lee, J. Lee, Y. Park, J. H. Kim, S.T. Shin, U.-H. Chung, Amorphous hafnium-indium-zinc oxide semiconductor thin film transistors, Appl. Phys. Lett. 95 (2009) 252103, https://doi.org/10.1063/1.3275801.
[12] J.C. Do, C.H. Ahn, H.K. Cho, H.S. Lee, Effect of Ti addition on the characteristics of titanium-zinc-tin-oxide thin-film transistors fabricated via a solution process, J. Phys. D: Appl. Phys. 45 (2012) 225103, https://doi.org/10.1088/0022-3727/45/22/225103.
[13] Y.-S. Shiah, K. Sim, Y. Shi, K. Abe, S. Ueda, M. Sasase, J. Kim, H. Hosono, Mobility-stability trade-off in oxide thin-film transistors, Nat. Electron. 4 (2021) 800–807, https://doi.org/10.1038/s41928-021-00671-0.
[14] H.Y. Jung, Y. Kang, A.Y. Hwang, C.K. Lee, S. Han, D.-H. Kim, J.-U. Bae, W.-S. Shin, J.K. Jeong, Origin of the improved mobility and photo-bias stability in a double-channel metal oxide transistor, Sci. Rep. 4 (2014) 3765, https://doi.org/10.1038/srep03765.
[15] M.H. Cho, C.H. Choi, J.K. Jeong, Comparative study of atomic layer deposited indium-based oxide transistors with a fermi energy level-engineered heterojunction structure channel through a cation combinatorial approach, ACS Appl. Mater. Interfaces 14 (2022) 18646–18661, https://doi.org/10.1021/acsami.1c23889.
[16] M. Furuta, D. Koretomo, Y. Magari, S.G.M. Aman, R. Higashi, S. Hamada, Heterojunction channel engineering to enhance performance and reliability of amorphous In-Ga-Zn-O thin-film transistors, Jpn. J. Appl. Phys. 58 (2019) 090604, https://doi.org/10.7567/1347-4065/ab1f9f.
[17] Y.-S. Kim, W.-B. Lee, H.-J. Oh, T.H. Hong, J.-S. Park, Remarkable stability improvement with a high-performance PEALD-IZO/IGZO top-gate thin-film transistor via modulating dual-channel effects, Adv. Mater. Interfaces 9 (2022) 2200501, https://doi.org/10.1002/admi.202200501.
[18] D. Khim, Y.-H. Lin, T.D. Anthopoulos, Impact of layer configuration and doping on electron transport and bias stability in heterojunction and superlattice metal oxide transistors, Adv. Funct. Mater. 29 (2019) 1902591, https://doi.org/10.1002/adfm.201902591.
[19] H. Faber, S. Das, Y.-H. Lin, N. Pliatsikas, K. Zhao, T. Kehagias, G. Dimitrakopulos, A. Amassian, P.A. Patsalas, T.D. Anthopoulos, Heterojunction oxide thin-film transistors with unprecedented electron mobility grown from solution, Sci. Adv. 3 (2017) e1602640, https://doi.org/10.1126/sciadv.1602640.
[20] Y.S. Rim, H. Chen, X. Kou, H.-S. Duan, H. Zhou, M. Cai, H.J. Kim, Y. Yang, Boost up mobility of solution-processed metal oxide thin-film transistors via confining structure on electron pathways, Adv. Mater. 26 (2014) 4273–4278, https://doi.org/10.1002/adma.201400529.
[21] Y.-H. Lin, H. Faber, J.G. Labram, E. Stratakis, L. Sygellou, E. Kymakis, N.A. Hastas, R. Li, K. Zhao, A. Amassian, N.D. Treat, M. Mclachlan, High electron mobility thin-film transistors based on solution-processed semiconducting metal oxide heterojunctions and quasi-superlattices, Adv. Sci. 2 (2015) 1500058, https://doi.org/10.1002/advs.201500058.

[22] J. Lee, J. Jin, S. Maeng, G. Choi, H. Kim, J. Kim, Enhancement of the electrical performance and bias stability of RF-sputtered indium tin zinc oxide thin-film transistors with vertical stoichiometric oxygen control, ACS Appl. Electron. Mater. 4 (2022) 1800–1806, https://doi.org/10.1021/acsaelm.2c00054.
[23] A. Abliz, D. Wang, L. Yang, M. Mamat, H. Chen, L. Xu, C. Wang, H. Duan, Investigation on the electrical performances and stability of W-doped ZnO thin-film transistors, Mater. Sci. Semicond. Process. 95 (2019) 54–58, https://doi.org/10.1016/j.mssp.2019.01.027.
[24] J.-I. Kim, K.H. Ji, H.Y. Jung, S.Y. Park, R. Choi, M. Jang, H. Yang, D.-H. Kim, J.-U. Bae, C.D. Kim, J.K. Jeong, Improvement in both mobility and bias stability of ZnSnO transistors by inserting ultra-thin InSnO layer at the gate insulator/channel interface, Appl. Phys. Lett. 99 (2011) 122102, https://doi.org/10.1063/1.3643054.
[25] G.G. Kumar, S. Kumaraguru, T. Partheeban, M. Sasidharan, V. Kumaran, P. Rajkumar, R. Subadevi, M. Sivakumar, R.M. Gnanamuthu, An enhanced electrochemical properties of novel tin based layered Li(Ni-Sn-Mn)O2 cathode material for rechargeable Li-ion batteries, Mater. Res. Express 6 (2019) 084007, https://doi.org/10.1088/2053-1591/ab2216.
[26] S. Parthiban, J.-Y. Kwon, Role of dopants as a carrier suppressor and strong oxygen binder in amorphous indium-oxide-based field effect transistor, J. Mater. Res. 29 (2014) 1585–1596, https://doi.org/10.1557/jmr.2014.187.
[27] H.Y. Chong, K.W. Han, Y.S. No, T.W. Kim, Effect of the Ti molar ratio on the electrical characteristics of titanium-indium-zinc-oxide thin-film transistors fabricated by using a solution process, Appl. Phys. Lett. 99 (2011) 161908, https://doi.org/10.1063/1.3655197.
[28] K. Joshi, M. Rawat, S.K. Gautam, R.G. Singh, R.C. Ramola, F. Singh, Band gap widening and narrowing in Cu-doped ZnO thin films, J. Alloys Compd. 680 (2016) 252–258, https://doi.org/10.1016/j.jallcom.2016.04.093.
[29] Q. You, H. Cai, Z. Hu, P. Liang, S. Prucnal, S. Zhou, J. Sun, N. Xu, J. Wu, Blue shift in absorption edge and widening of band gap of ZnO by Al doping and Al-N co-doping, J. Alloys Compd. 644 (2015) 528–533, https://doi.org/10.1016/j.jallcom.2015.05.060.
[30] Y. Kim, W. Lee, D.-R. Jung, J. Kim, S. Nam, H. Kim, B. Park, Optical and electronic properties of post-annealed ZnO:al thin films, Appl. Phys. Lett. 96 (2010) 171902, https://doi.org/10.1063/1.3419859.
[31] M.P.S. Rana, R. Singh, S. Negi, S.K. Gautam, R.G. Singh, R.C. Ramola, Band gap engineering and low temperature transport phenomenon in highly conducting antimony doped tin oxide thin films, Ceram. Int. 42 (2016) 5932–5941, https://doi.org/10.1016/j.ceramint.2015.12.141.
[32] T.P. Rao, M.C.S. Kumar, S.A. Angayarkanni, M. Ashok, Effect of stress on optical band gap of ZnO thin films with substrate temperature by spray pyrolysis, J. Alloys Compd. 485 (2009) 413–417, https://doi.org/10.1016/j.jallcom.2009.05.116.
[33] Y. Jung, W. Yang, C.Y. Koo, K. Song, J. Moon, High performance and high stability low temperature aqueous solution-derived Li-Zr co-doped ZnO thin film transistors, J. Mater. Chem. 22 (2012) 5390–5397, https://doi.org/10.1039/C2JM15526E.
[34] Q. Zhu, J. Lu, Y. Wang, F. Qin, Z. Shi, C. Xu, Burstein-Moss effect behind Au surface plasmon enhanced intrinsic emission of ZnO microdisks, Sci. Rep. 6 (2016) 36194, https://doi.org/10.1038/srep36194.
[35] J. Wang, Z. Wang, B. Huang, Y. Ma, Y. Liu, X. Qin, X. Zhang, Y. Dai, Oxygen vacancy induced band-gap narrowing and enhanced visible light photocatalytic activity of ZnO, ACS Appl. Mater. Interfaces 4 (2012) 4024–4030, https://doi.org/10.1021/am300835p.
[36] H. Liu, F. Zeng, Y. Lin, G. Wang, F. Pan, Correlation of oxygen vacancy variations to band gap changes in epitaxial ZnO thin films, Appl. Phys. Lett. 102 (2013) 181908, https://doi.org/10.1063/1.4804613.
[37] J. Yao, N. Xu, S. Deng, J. Chen, J. She, H.-P.D. Shieh, P.-T. Liu, Y.-P. Huang, Electrical and photosensitive characteristics of a-IGZO TFTs related to oxygen vacancy, IEEE Trans. Electron. Devices 58 (2011) 1121–1126, https://doi.org/10.1109/TED.2011.2105879.
[38] M. Ishfaq, M.R. Khan, M.F. Bhopal, F. Nasim, A. Ali, A.S. Bhatti, I. Ahmed, S. Bhardwaj, C. Cepek, 1.5MeV proton irradiation effects on electrical and structural properties of TiO2/n-Si interface, J. Appl. Phys. 115 (2014) 174506, https://doi.org/10.1063/1.4874942.
[39] T. Kamiya, K. Nomura, H. Hosono, Present status of amorphous In-Ga-Zn-O thin-film transistors, Sci. Technol. Adv. Mater. 11 (2010) 044305, https://doi.org/10.1088/1468-6996/11/4/044305.
[40] B. Babu, I.N. Reddy, K. Yoo, D. Kim, J. Shim, Bandgap tuning and XPS study of SnO2 quantum dots, Mater Lett 221 (2018) 211–215, https://doi.org/10.1016/j.matlet.2018.03.107.
[41] C. Fonseca, S. Boudin, M.C. Belo, Characterisation of titanium passivation films by in situ ac impedance measurements and XPS analysis, J. Electroanal. Chem. 379 (1994) 173–180, https://doi.org/10.1016/0022-0728(94)87136-1.
[42] K. Takechi, Y. Kuwahara, J. Tanaka, H. Tanabe, Depth-profiling XPS analysis of He-plasma treated amorphous InGaZnO thin films for use in top-gate coplanar thin-film transistors, Jpn. J. Appl. Phys. 58 (2019) 038005, https://doi.org/10.7567/1347-4065/aafed3.
[43] Z. Yang, J. Yang, T. Meng, M. Qu, Q. Zhang, Influence of channel layer thickness on the stability of amorphous indium zinc oxide thin film transistors, Mater Lett 166 (2016) 46–50, https://doi.org/10.1016/j.matlet.2015.12.029.
[44] G. Horowitz, Interfaces in organic field-effect transistors, organic electronics, Adv. Polymer Sci. 223 (2009) 113–153, https://doi.org/10.1007/12_2009_7.
[45] J.K. Jeong, Photo-bias instability of metal oxide thin film transistors for advanced active matrix displays, J. Mater. Res. 28 (2013) 2071–2084, https://doi.org/10.1557/jmr.2013.214.
[46] H.J. Seul, J.H. Cho, J.S. Hur, M.H. Cho, M.H. Cho, M.T. Ryu, J.K. Jeong, Improvement in carrier mobility through band-gap engineering in atomic-layer-deposited In-Ga-Zn-O stacks, J. Alloys Compd. 903 (2022) 163876, https://doi.org/10.1016/j.jallcom.2022.163876.
[47] Y.-S. Shiah, K. Sim, S. Ueda, J. Kim, H. Hosono, Unintended carbon-related impurity and negative bias instability in high-mobility oxide TFTs, IEEE Electron Device Lett 42 (2021) 1319–1322, https://doi.org/10.1109/LED.2021.3101654.
[48] K. Ide, Y. Kikuchi, K. Nomura, M. Kimura, T. Kamiya, H. Hosono, Effects of excess oxygen on operation characteristics of amorphous In-Ga-Zn-O thin-film transistors, Appl. Phys. Lett. 99 (2011) 093507, https://doi.org/10.1063/1.3633100.
[49] Y.J. Tak, S.T. Keene, B.H. Kang, W.-G. Kim, S.J. Kim, A. Salleo, H.J. Kim, Multifunctional, room-temperature processable, heterogeneous organic passivation layer for oxide semiconductor thin-film transistors, ACS Appl. Mater. Interfaces 12 (2020) 2615–2624, https://doi.org/10.1021/acsami.9b16898.
[50] Y. Kikuchi, K. Nomura, H. Yanagi, T. Kamiya, M. Hirano, H. Hosono, Device characteristics improvement of a-In-Ga-Zn-O TFTs by low-temperature annealing, Thin Solid Films 518 (2010) 3017–3021, https://doi.org/10.1016/j.tsf.2009.10.132.
[51] R.N. Bukke, C. Avis, J. Jang, Solution-processed amorphous In-Zn-Sn oxide thin-film transistor performance improvement by solution-processed Y2O3 passivation, IEEE Electron Device Lett 37 (2016) 433–436, https://doi.org/10.1109/LED.2016.2528288.
[52] H.-S. Jeong, H.-S. Cha, S.-H. Hwang, D.-H. Lee, S.-H. Song, H.-I. Kwon, Effects of oxygen content on operational characteristics and stability of high-mobility IGTO thin-film transistors during channel layer deposition, Coatings 11 (2021) 698, https://doi.org/10.3390/coatings11060698.
[53] Z. Zhang, J. Huang, B. Dong, Q. Yuan, Y. He, O.S. Wolfbeis, Rational tailoring of $ZnSnO_3/TiO_2$ heterojunctions with bioinspired surface wettability for high-performance humidity nanosensors, Nanoscale 7 (2015) 4149–4155, https://doi.org/10.1039/C4NR07559E.
[54] W. Zhong, L. Kang, S. Deng, L. Lu, R. Yao, L. Lan, H.S. Kwok, R. Chen, Effect of Sc2O3 passivation layer on the electrical characteristics and stability of InSnZnO thin-film transistors, IEEE Trans. Electron. Devices 68 (2021) 4956–4961, https://doi.org/10.1109/TED.2021.3105486.